iJRASET
International Journal For Research in Applied Science and Engineering Technology

INTERNATIONAL JOURNAL FOR RESEARCH

IN APPLIED SCIENCE & ENGINEERING TECHNOLOGY

Volume: 13 **Issue:** X **Month of publication:** October 2025

DOI: https://doi.org/10.22214/ijraset.2025.74837

www.ijraset.com

Call: 08813907089 | E-mail ID: ijraset@gmail.com

International Journal for Research in Applied Science & Engineering Technology (IJRASET)
ISSN: 2321-9653; IC Value: 45.98; SJ Impact Factor: 7.538
Volume 13 Issue X Oct 2025- Available at www.ijraset.com

CFD Analysis of Dirty-Air Reduction with Diverse Rear Wing Topologies

Abhinav Sharma[1], Rishi Gupta[2], Diksha Khuas[3]
[1, 2, 3]*Independent Researcher,* [1,3]*40 Pleydell Close, Coventry, United Kingdom,* [2]*Flat 9 Charter House, 426 Avebury Boulevard, Milton Keynes, United Kingdom*

Abstract: ***This study investigates how rear-wing topology influences wake quality and dirty-air generation in a tandem configuration using numerical simulations in STAR-CCM+. A series of wing geometries with varying endplate angles and size ratios were analysed to understand their impact on aerodynamic loading, flow coherence, and overall system efficiency.Results show that increasing suction on the leading wing improves its aerodynamic performance but simultaneously intensifies the wake, creating a stronger low-energy region that degrades the follower's inflow quality. In contrast, moderate endplate angling up to 8 degrees and controlled downsizing were found to narrow the wake corridor, enhance total-pressure recovery, and reduce dirty-air severity. The findings highlight that no single geometry can optimise both wings simultaneously: designs favouring the leader tend to compromise the follower. Configurations that balance geometry and wake management, however, achieve cleaner inter-element flow and improved overall efficiency. These insights provide a foundation for future aerodynamic co-optimisation of multi-element systems where wake control and stability are critical.***
Keywords: Dirty Air, Aerodynamic Performance, CFD, Rear Wing Topologies, Wake

I. INTRODUCTION

Aerodynamics is crucial to a formula car's competitiveness and the single most key area for improvement. Downforce and drag are the two paramount aerodynamic forces[1]. Downforce is the force component that seeks to press a vehicle into the ground and allow the formula car to withstand high velocity turns and improved traction through acceleration. Furthermore, drag force acts as the resistive force attempting to decelerate the formula car. As a result, the aerodynamic designer is concerned with two key issues: increasing downforce and lowering drag, simultaneously. The rear wing, on the other hand, is a significant component of aerodynamics. To maintain the vehicle's handling and balance, the rear wings often generate more than twice as much downforce as the front wings, but this varies on the type of formula car and its applications[2]. The rear wing experiences relatively 'clean' airflow because it is placed higher than bodywork parts to obtain access to undistributed airflow[3].

In the modern era of Formula 1, governing bodies have sought designs that allow closer racing by reducing the strength and sensitivity of the turbulent wake[4]. A following car can suffer large downforce losses in the leader's wake, with substantial performance degradation reported in prior analyses[5].

Clean air denotes unobstructed freestream ahead of a car; dirty air denotes the turbulent, energy-deficient wake shed by a car ahead. Aero surfaces generate less downforce in this turbulent inflow, and the deficit grows as the following distance shrinks[5]. Although recent regulations aim to reduce wake sensitivity[4], the coupling between wake width/strength and following losses remains a central challenge[5].

Aerodynamic surfaces lose efficiency in turbulent air, generating progressively less downforce as the following car approaches the one ahead. In recent analyses, Formula 1 reported that a car following at 20 m can experience around a one-third reduction in downforce, increasing to nearly half at 10 m separation. The 2022 regulations were introduced to counter this effect by designing cars that produce cleaner wakes and are less sensitive to turbulent inflow. Although turbulent wakes have always challenged drivers, their intensity and width have increased in the past decade due to aerodynamic out-washing, making close racing more difficult.

In open-wheel racing, a car's aerodynamic design influences not only its overall performance but also its interaction with other cars on the track. As aerodynamic technology has advanced, the issue of dirty air—the turbulent wake created by a leading car—has become a significant obstacle to close racing. The car following behind suffers notable decreases in downforce and stability due to this disturbed airflow, which changes the pressure and velocity patterns over key aerodynamic components like the front and rear wings. Effectively managing this interaction is therefore crucial to maintain aerodynamic efficiency and consistent handling under different flow conditions.

Recent Formula One regulation changes have sought to reduce wake sensitivity by simplifying car geometries and redesigning underfloor tunnels. However, the rear wing continues to be a major source of wake generation because of its high-pressure differences and strong tip vortices. Research by Newbon and Sims-Williams [6] and Wilson et al.[5] emphasizes that the rear wing's shape—especially the design of the endplates and the spanwise dimensions—significantly influences the width of the wake and the downstream pressure deficit. Despite these insights, there has been limited research quantifying how small geometric modifications affect wake coherence and the aerodynamic performance of the trailing car in realistic tandem setups.

This study aims to fill this gap by investigating how changes in rear-wing design impact wake behaviour and the severity of dirty air in a two-car configuration. Twelve different wing geometries were simulated in STAR-CCM+, incorporating systematic variations in endplate angle and wing size. By assessing downforce, drag, and total-pressure recovery, the study seeks to identify wing configurations that strike an optimal balance between aerodynamic efficiency for the leading car and reduced wake disruption for the car behind. The results enhance understanding of the aerodynamic compromises inherent in race-car design and offer a basis for future co-optimisation of multi-element aerodynamic systems.

The aerodynamic wake produced by a Formula 1 rear wing is inherently complex, featuring strong vortex structures and low-energy recirculation zones[3]. These characteristics not only affect the pressure field behind the car but also influence the performance of aerodynamic components on the following car when operating within the wake. Prior numerical and experimental work has shown that altering endplate shape or wingspan can change the intensity and path of these vortices, directly affecting total-pressure recovery and wake diffusion rates[5], [7]. Building on this knowledge, the current research examines how various rear-wing designs interact under consistent boundary conditions and flow speeds.

From a wider engineering perspective, understanding dirty-air effects has relevance beyond motorsport. The same aerodynamic principles apply to vehicle platooning, multi-aircraft formations, and high-efficiency transport design, where wake-induced interference significantly impacts system performance. By exploring the aerodynamic interaction between leading and trailing elements, this research provides insights into how geometric adjustments can reduce negative wake effects, enhance flow coherence, and improve overall energy efficiency([8], [9]). Consequently, the findings can inform not only competitive race-car design but also broader aerodynamic optimisation strategies across advanced mobility fields.

Although significant advancements have been made in numerical simulations and experimental wind-tunnel testing, a consistent discrepancy remains between simplified models and the actual behaviour of full-scale wakes. Simplified geometries frequently fail to represent the coupled flow phenomena caused by real-world turbulence intensity, wall interference, and Reynolds number effects ([10], [11]). As highlighted by Hughes[11], computational analyses based on idealised models tend to underestimate wake diffusion and overestimate aerodynamic stability, emphasising the need for mesh-independence and turbulence-model validation. To address this challenge, the current study uses a high-fidelity CFD framework that combines transient turbulence modelling with mesh-refinement validation, ensuring a more accurate representation of aerodynamic performance in racing contexts. This method, aligned with best practices suggested in recent aerodynamic assessments [9], increases confidence in the reliability of the aerodynamic metrics obtained.

Moreover, wake dynamics are inherently non-linear, with minor geometric changes causing significant variations in vortex strength, downwash direction, and induced drag ([3], [6]). Investigating this sensitivity is crucial to understanding why some wing configurations perform well individually but degrade when used together. Previous research has demonstrated that slight adjustments in endplate geometry or chord length can notably alter vortex paths and wake coherence([5], [7]). By analysing multiple configurations of both leading and trailing wings, this study identifies not only which designs reduce dirty-air effects but also how their flow structures develop spatially within the wake field.

Ultimately, the insights gained from this research aim to support aerodynamic co-design strategies that improve both performance and race ability. Achieving high aerodynamic efficiency while maintaining stable wake behaviour contributes to safer and more competitive racing environments. Over time, these findings could influence future Formula One regulations and guide engineers toward design philosophies that balance individual vehicle performance with the collective aerodynamic conditions of the racing field.

II. GOVERNING EQUATIONS

In essence, Computational Fluid Dynamics (CFD) is a numerical simulation that utilizes algorithms to tackle aerodynamic problems involving fluid flow. Nowadays, computers manage the millions of calculations required to replicate the real-world interaction between a fluid and an object.

The CFD process itself involves three stages: pre-processing, solving partial differential equations, and post-processing[8]. The first and last steps, pre-processing and post-processing, are relatively straightforward and involve setting parameters within a CFD software's graphical interface.

CFD boasts a wide range of applications in automotive design, particularly where aerodynamics plays a critical role. It empowers engineers to make computational estimations of a design's effects. Consequently, engineers can adjust and modifications earlier in the design phase, rather than having to modify a prototype after wind tunnel testing. This early problem-solving capability is a major advantage of CFD. Furthermore, the ability to obtain data without physically constructing a prototype model significantly reduces production costs. For these reasons, CFD is widely used by racing teams worldwide. However, it is not without its drawbacks. Utilizing CFD requires an investment, as extensive resources are necessary to analyze the complex, separated flows associated with a Formula One car.

A. Navier-Stokes Equations

The Navier-Stokes equations, represented by equations (1.1 a-c), stem from applying Newton's second law of motion to fluid flow[8]. These momentum equations are then refined by incorporating the characteristics of a Newtonian fluid. Newtonian fluids exhibit a simple relationship between their viscosity and their deform rate. By incorporating this assumption -- that viscous stresses are proportional to the rates of deformation[1] -- into the initial momentum equations, we arrive at the final form of the Navier-Stokes equations.

$$\frac{\partial(pu)}{\partial t} + div(pu\upsilon) = -\frac{\partial p}{\partial x} + div(\mu.grad.u) + S_{m_x} \qquad \text{Eq. (1.1 (a))}$$

$$\frac{\partial(pu)}{\partial t} + div(pv\upsilon) = -\frac{\partial p}{\partial y} + div(\mu.grad.v) + S_{m_y} \qquad \text{Eq. (1.1 (b))}$$

$$\frac{\partial(pw)}{\partial t} + div(pw\upsilon) = -\frac{\partial p}{\partial z} + div(\mu.grad.w) + S_{m_z} \qquad \text{Eq. (1.1 (c))}$$

where p is the density, velocity vector u= [u v w], mu is the viscosity and P is the pressure. Where the Fourth row is the rate of momentum increase due to sources, the Third row is the rate of momentum increase due to diffusion, whereas the Second is the net rate of momentum out of fluid element, and the First is the rate of fluid Momentum increase.

$$\frac{\partial\rho}{\partial x} + div(\rho u) = 0 \qquad \text{Eq. (1.2)}$$

Equation (1.2), which derives from the rule of conservation of mass, illustrates the continuity equation for a compressible fluid. It maintains the mass constant in the system, implying that fluids cannot be generated in an element or vanish on their own. The mass flow through the cell and the rate of pressure change are balanced by the formula.

$$\frac{\partial(\rho i)}{\partial t} + div(pi\upsilon) = -p.div.u + div(KgradT) + D + S_i \qquad \text{Eq. (1.3)}$$

The energy equation in (1.3) is similar to equation (1.1) in terms of the term structure, but it pertains to energy balancing, which is the goal of energy conservation in the system while taking temperature, pressure, and internal energy into account.

B. Reynolds Averaged Navier-Stokes (RANS)

The Reynolds decomposition of velocity in turbulent flow can be broken down into two parts[1], mean velocity and fluctuation velocity. Although there have been fewer studies on fluctuation flow, the means are often of more interest because of certain characteristics that the fluctuations flow brings that cannot be disregarded. The RANS equations (1.4 a-c) come from introducing the Reynolds decomposition to the original Navier-Stokes equations (1.1), followed by a time average of the expressions.

$$\frac{\partial(\overline{\rho}U)}{\partial t} + div(\overline{\rho}UU) = -\frac{\partial\overline{P}}{\partial y} + div(\mu gradU) + \left[-\frac{\partial\left(\overline{pu^2}\right)}{\partial x} - \frac{\partial\left(\overline{\rho u'v'}\right)}{\partial y} - \frac{\partial\left(\overline{\rho u'w'}\right)}{\partial x} + S_{M_x}\right] \qquad \text{Eq. (1.4 (a))}$$

$$\frac{\partial(\overline{\rho}V)}{\partial t} + div(\overline{p}VU) = -\frac{\partial \overline{P}}{\partial x} + div(\mu gradV) + \left[-\frac{\partial\left(\overline{\rho u'v'}\right)}{\partial x} - \frac{\partial\left(\overline{\rho v'^2}\right)}{\partial y} - \frac{\partial\left(\overline{\rho v'w'}\right)}{\partial z} + S_y \right] \quad \text{Eq. (1.4 (b))}$$

$$\frac{\partial(\overline{\rho}W)}{\partial t} + div(\overline{p}WU) = -\frac{\partial \overline{P}}{\partial z} + div(\mu gradW) + \left[-\frac{\partial\left(\overline{\rho u'w'}\right)}{\partial x} - \frac{\partial\left(\overline{\rho v'w'}\right)}{\partial y} - \frac{\partial\left(\overline{\rho w'^2}\right)}{\partial z} + S_{M_x} \right] \quad \text{Eq. (1.4 (c))}$$

The outcome appears to be the regular Navier-Stokes with the mean velocity U replacing the regular velocity U, plus the sum of three additional terms known as Reynold stresses. These are the remaining characteristics of the fluctuations flow that have a significant impact on turbulent flow but have proven to be extremely difficult to measure.

C. RANS turbulence Model

The function of a RANS turbulence model is to convert and streamline the Reynold stresses' effects into the time-averaged Navier-Stokes formula. Since it would be extremely expensive and hard to recreate the physical flow that the Reynold stresses provide, the stress words are substituted with models that depict the consequences of the Reynold stresses.

The Boussinesq proposition, which derives from the theory that they are proportionate to mean rates of deformation, is used to construct the Reynolds shear stresses.

$$\rho\overline{u_i u_j} = \mu_t\left(\frac{\partial U_i}{\partial x_j} + \frac{\partial U_j}{\partial x_i}\right) - \frac{2}{3}\rho k\delta_{ij} \quad \text{Eq. (1.5)[1]}$$

Where μ_t the turbulence viscosity$k = \frac{1}{2}\left(\overline{u'^2} + \overline{v'^2} + \overline{W'^2}\right)$, is the turbulence kinetic energy per unit mass, and the Kronecker delta, whether to calculate for shear stress or normal.

III. METHODOLOGY AND DATA PREPARATION

A. Mesh Independence Analysis

A mesh-independent solution ensures that key outputs (e.g., coefficients, pressure distributions) no longer change materially with further refinement. Guidance for external automotive aerodynamics and F1 contexts motivates structured refinement and domain sizing [10]. Validation studies on simplified car geometries comparing turbulence models (e.g., standard k–ε and SST k–ω) inform model selection and expectations[11], while comparative work on meshing strategies supports the use of multiple techniques and cross-checks [9].

In this study, the conventional k–ε and SST (Shear Stress Transport) models were applied to a rear wing at a uniform inlet velocity V_n = 50 m/s [9]. Very fine meshes reduce numerical error but raise cost steeply; hence a graded refinement was used to identify the smallest mesh that stabilizes Cd/Cl trends **(**[9], [10]**)**.

TABLE I
C_d Value for Various Mesh Configurations

Configuration	Very Coarse	Coarse	Medium	Fine	Very Fine	Ultra Fine
Total Number of Mesh Cells	361449	5288225	9607985	12163996	14430302	20000000
Cd in Iteration	0.3911	0.3738	0.3670	0.3525	0.3510	0.3509

TABLE II
Convergence Time for Various Cell Configurations

Mesh Type	Cell Count	Average Time for One Simulation Converge
Polyhedral	Very Coarse (3614494)	5 Hours

	Coarse (5288225)	8 Hours
	Medium (9607985)	14 Hours
	Fine (12163996)	20 Hours
	Very-Fine(14430302)	24 Hours
	Ultra-Fine (20000000)	32 Hours

To forecast the downforce, lift coefficients, and drag on normalized mesh cells to ascertain how the mesh quality impacts CFD simulation results.Five alternative meshes; coarse, medium, fine, very fine, and ultra-fine gridwere developed for each of the mesh cases taken for the leading rear wing. This study was done to establish and analyse the airflow around the rear of the car, a mesh-independent study was carried out. Table (I) highlights the results against the mesh quality as well as the number of nodes and duration of simulation for the mesh cases that were simulated. Table (II) contains the data captured by using the regular k-model. K-ε was consistently the most accurate of the three models in both C_L (Coefficient of Lift) and C_D (Coefficient of Drag) prediction and drag contribution. However, in most cases, K- ω results show a similar pattern to K- ε, yet with a slightly larger error percentage. The important mesh properties are summarised in Table (III), and it is abundantly obvious that the length of a CFD simulation depends significantly on the number of mesh nodes considered. Furthermore,[10] discovered that the huge dimensions, particularly the 8L length, (where L is the length along the x-axis (forward direction)), result in an impractically prolonged period between each iteration. As a result, to prevent memory and time-consuming issues, a mesh-independent analysis was conducted using a strategic method to employ the highest and the most appropriate mesh model to analyse the airflow around the car.

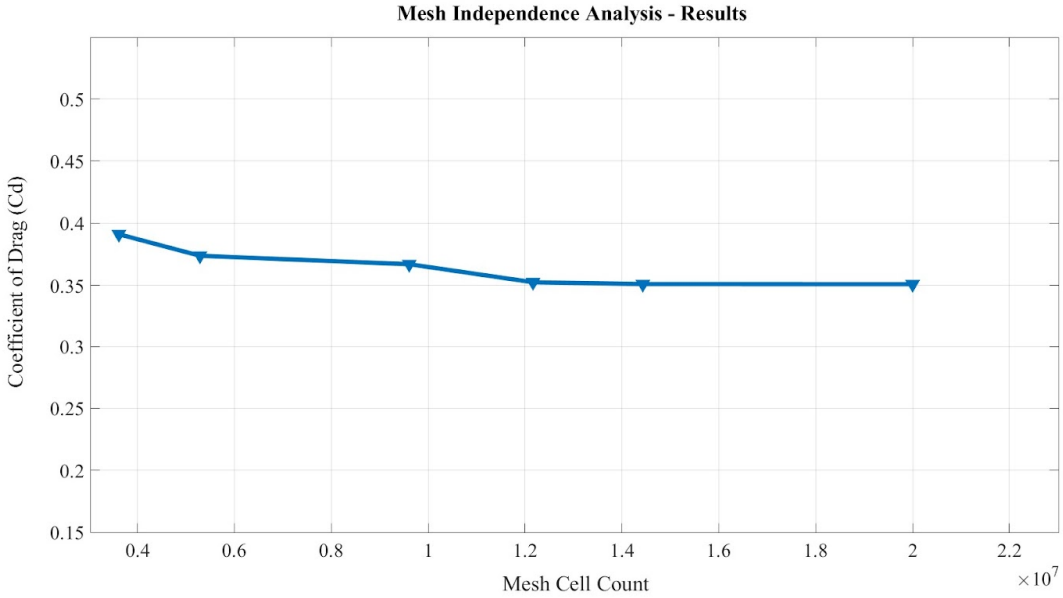

Fig.1 Mesh Independence Analysis Results Plot

As from the Fig.1 which represents the results of mesh independence analysis, it can be clearly inferred that mesh cell counts beyond $1.2x10^7$does not yield any further improvement in the value of coefficient of drag. Therefore, to use the balance between computation time and best mesh cell count for the topology, the mesh cell counts of $1.2x10^7$was used in the simulations.

B. Wind Tunnel Modelling

[12]The MIRA closed wind tunnel testing was adopted in this study. It had a domain wind tunnel length of 15m, a height of 2.2m, and a width of 2.4m which was designed using StarCCM+[13]. The tunnel was modelled as a closed, stationary, no-slip enclosure with specified inlet velocity and pressure outlet. The baseline leading rear wing area was 0.147 m²; the tunnel cross-section area was 5.28 m² with a blocking factor of 2.78%. For contextual speeds and downforce magnitudes often quoted in F1 coverage, we referenced prior summaries to choose a representative 50 m/s inlet for the present simulations [14].

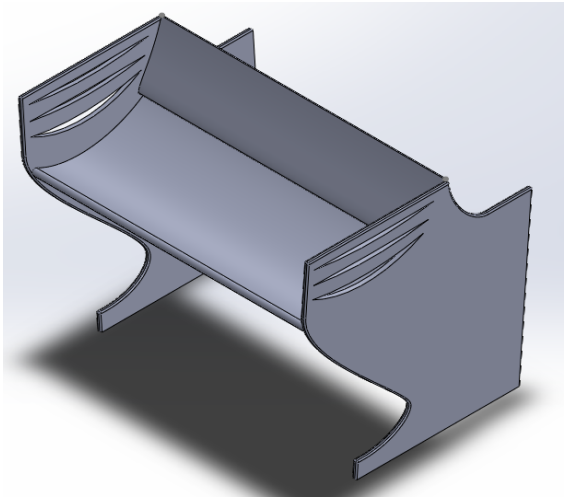

Fig.2 Unmodified Leading Rear Wing

The fundamental purpose of the aerodynamics in racing is to increase the downforce acting on the vehicle, with the least magnitude of drag possible. Without aerodynamic downforce, these cars generate enough lift to “fly” while traveling at 160 kph (100 mph) alone. Considering, Formula 1 race cars usually race at an average speed of 300 kph (185 mph)[14]. This culminates where the “rubber hits the road” and gives traction to the tires to travel at immense speeds and high g’s (acceleration of gravity). With aerodynamic downforce, at top speed a Formula 1 race car can achieve a downforce of 2.5 times the car’s weight [14]

However, with the literature survey the average speed around the racetracks was found to be "300kph (185mph)". Therefore, the same speed value was used for simulations in our study, a vehicle velocity of 50m/s.The inlet velocity was a free stream with a magnitude of V= 50 m/s and a turbulent intensity setup of 0.01 %. This setup helped to analyze and better understand the behaviour of each force components of the primary aerodynamic component, the modified leading rear, along with other coefficients.

In this study, a wind tunnel setup with 2 rear wings was modelled to replicate a close racing scenario. The gap between the leading car’s rear wing and the trailing car’s rear wing was set to 5m[5].The position of the leading car was placed at one car length (3.6m) from the inlet of the domain of wind tunnel. The distance between the two cars was measured from the rear end of the leading car to the rear end of the trailing car which equals 5m in length. For a long time, the FIA and Formula One have been collaborating to develop a car that can race more closely. To achieve a closer racing car, the leading car should produce the least amount of turbulent (dirty) wake. In a Formula One racing car scenario, the second car will lose 40% of its downforce due to the lead car's foul air [5], [10].

When a car's aerodynamic systems cause the air to pass through, the airflow loses energy and results in low velocity, which was one of the reasons for turbulence. This turbulence when reaches the end of the rear wing, transforms into a turbulent raging mushroom wake. The lead car's hot, turbulent mushroom wake is termed the cruise control effect, which occurs mostly in the straights.

C. Mesh Properties for Wind Tunnel Modelling

The mesh generated for the simulations was done with the following settingparameters mentioned in Table (III). For meshing properties, a polyhedral mesh setup was used which was deployed and suggested by many authors in their research studies[9], [15]. The primary reason for this was that a polyhedral mesh was less time consumable and was simpler than any other mesh type. Additionally, it creates hexagonal shape cells, perfect for complicated CAD profiles with refined mesh. The same mesh profile was then used to investigate the leading modified rear wing’s aerodynamic performance.

TABLE III
Mesh Properties Parameters

Base Size	0.1m
Target surface size (% relative to bass size)	6.0

Minimum surface size (% relative to bass size)	1.0
Surface curvature (points/circle)	200
Number of prism layer	2
Prism layer stretching	1.2
Prism layer thickness	5.0
Volume Growth rate	2.0

D. Modification Matrix of Leading Rear Wing

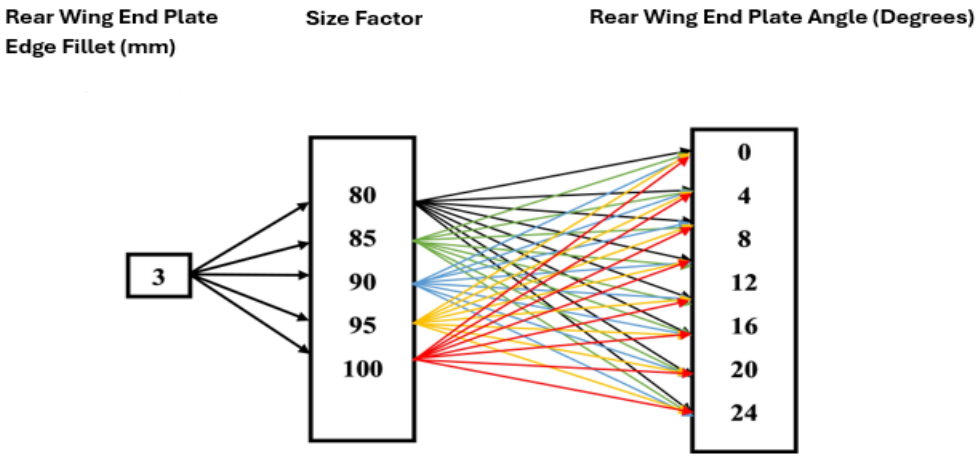

Fig.3 Modification Matrix of Leading Rear Wing

This study analysed two configurations of the 2021 Formula one rear wing: a leading modified rear wing and an unmodified trailing rear wing. The unmodified wing represents the baseline 2021 design, which generates strong tip vortices and turbulent wakes due to its larger size and sharper aerodynamic features[7]. These vortices create "dirty air"—disrupted airflow that destabilizes following cars. The modified rear wing was scaled down iteratively from 100% (original size) to 80% in 5% increments. This size reduction directly weakens the tip vortices by reducing the wing's span and chord length, which lowers the energy of rotating airflow at the endplates[16]. The edge fillet radius was fixed at 3 mm (vs. the sharper baseline edge) to smooth airflow separation, while the end plate angle was adjusted to redirect vortices upward and laterally, similarly can be found in Figure3 which dictated the modification Matrix of leading rear wing. These geometric changes minimize the intensity and spatial spread of turbulent wakes[17].

In contrast, the unmodified trailing wing retains its original dimensions and sharper edges, producing stronger, more coherent vortices. These vortices persist longer in the wake, creating larger low-pressure zones that degrade the aerodynamic performance of trailing cars. By scaling and refining the leading wing's geometry, the study aims to reduce dirty air's destabilizing effects, enabling closer racing and improved overtaking opportunities.

Figure 3 illustrates the Modification Matrix of the leading rear wing, highlighting key geometric adjustments and their role in reducing dirty air.To achieve these objectives, a wind tunnel simulation was developed in Star CCM+, utilizing unmodified 2021 Formula one rear wings under controlled conditions. The simulation setup adhered to standardized parameters, ensuring consistency in airflow conditions and boundary constraints. By placing two identical rear wings from the same car in a tandem configuration, the aerodynamic interactions between the leading and trailing wings could be systematically analyzed. The leading wing was then subjected to a series of geometric modifications, forming what is now referred to as the modified leading rear wing. These modifications, outlined in the Change Matrix (Figure 3), were designed to evaluate their influence on vortex formation and wake turbulence.

TABLE IV
Wing Topology Label Map

Alphabet	Topology Combination
A	RW_3 mm_100p_0d
B	RW_ 3 mm_100p_8d
C	RW_3 mm_100p_ 16d
D	RW_3 mm_100p_24d
E	RW_3 mm_90p_0d
F	RW_3 mm_90p_8d
G	RW_3 mm_90p_16d
H	RW_3 mm_90p_24d
I	RW_3 mm_80p_0d
J	RW_3 mm_80p_8d
K	RW_3 mm_80p_16d
L	RW_3 mm_80p_24d

Once the simulations were completed for all wing configurations, performance data was collected for both the leading and trailing wings. The analysis aimed to determine the optimal modifications that would minimize dirty air without significantly compromising the aerodynamic efficiency of the leading wing. The primary objective was to reduce wake turbulence in a way that enhanced the performance of the trailing wing, facilitating better aerodynamic conditions for following cars. The ideal configuration would achieve a balance where the leading wing experiences minimal performance loss while the trailing wing benefits from improved downforce retention and reduced aerodynamic disruption. By methodically testing and analysing these wing configurations, this study provides valuable insights into how rear-wing design can be optimized to mitigate dirty air, ultimately contributing to closer racing dynamics and improved overtaking opportunities in Formula one.

Twelve different rear wing topologies were analysed under varying dirty air conditions[18], with each setup of combination labelled alphabetically from A to L, as seen in Table (IV) and Figures (4,5,6 and 7). This was done to have clarity across all result plots. In all visualizations, blue represents the leading wing, and orange represents the trailing wing. This colour scheme is consistently applied to all parameters, shown in Figures (4-7), including downforce, drag force, lift coefficient (C_l), and drag coefficient (C_d). The results demonstrate how each wing element behaves individually under different percentage reductions and positional offsets. This approach allows for easy visual comparison and helps identify how dirty air affects aerodynamic performance across various wing configurations. The breakdown of topology combination as in Table (IV) is as follows, RW represents rear wing, followed by 3mm which is the fillet size (fixed) followed by the size percentage of rear end plate (100p=100%, 90p=90% and 80p=80%) and finally the rear end plate angle in degrees (0d, 8d, 16d, and 24d which is 0 degrees, 8 degrees, 16 degrees and 24 degrees respectively).

The following graphs in Figures (4,5,6 and 7) summarizes the simulation results for different rear wing configurations tested in STAR-CCM+, focusing on evaluating aerodynamic performance through drag coefficient (C_d), lift coefficient (C_l), downforce, and drag force. Various modifications, including changes in the size factor, end plate edge fillet, and rear wing end plate angle, were investigated to determine their impact on aerodynamic efficiency and stability. The nomenclature used for each configuration follows a structured format, where the end plate edge fillet radius (in mm), size factor (as a percentage), and rear wing end plate angle (in degrees) define the setup. The fillet size influences airflow smoothness, reducing local flow separation, while the size factor dictates overall wing scaling, affecting drag and lift. The rear wing end plate angle guides airflow and alters vortex strength, significantly impacting aerodynamic efficiency. Simulations were conducted for both leading and trailing rear wings to analyze their combined effect on downforce generation and wake turbulence.

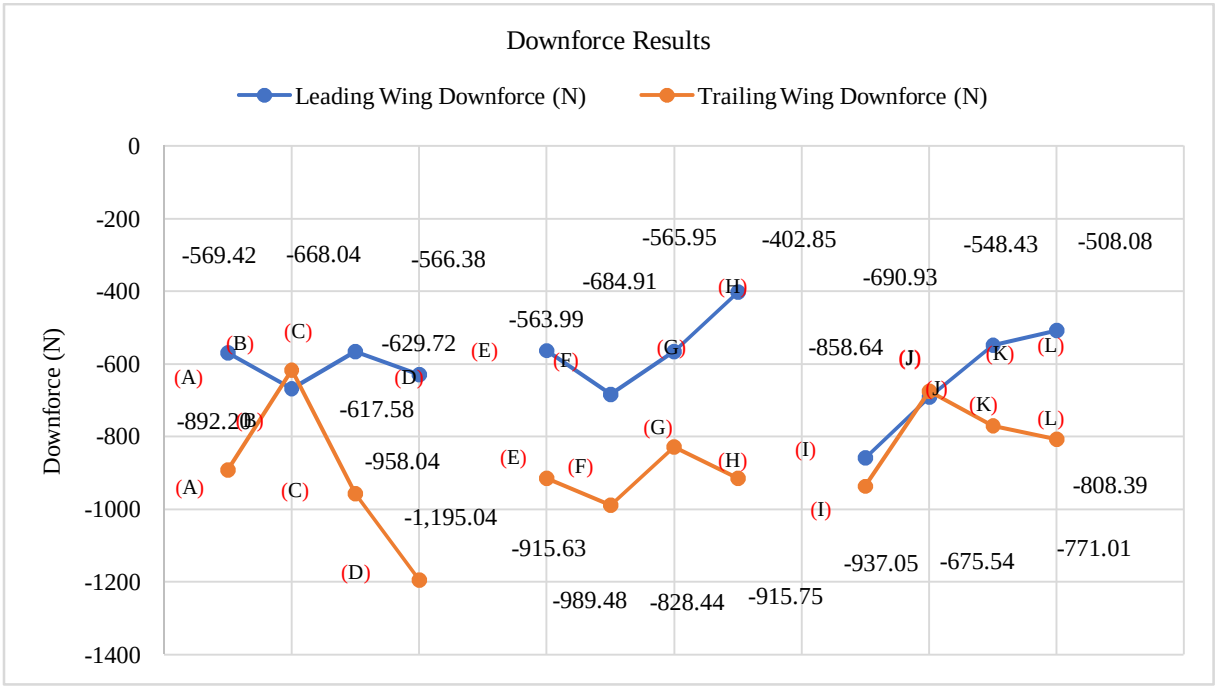

Fig.4Results of Downforce

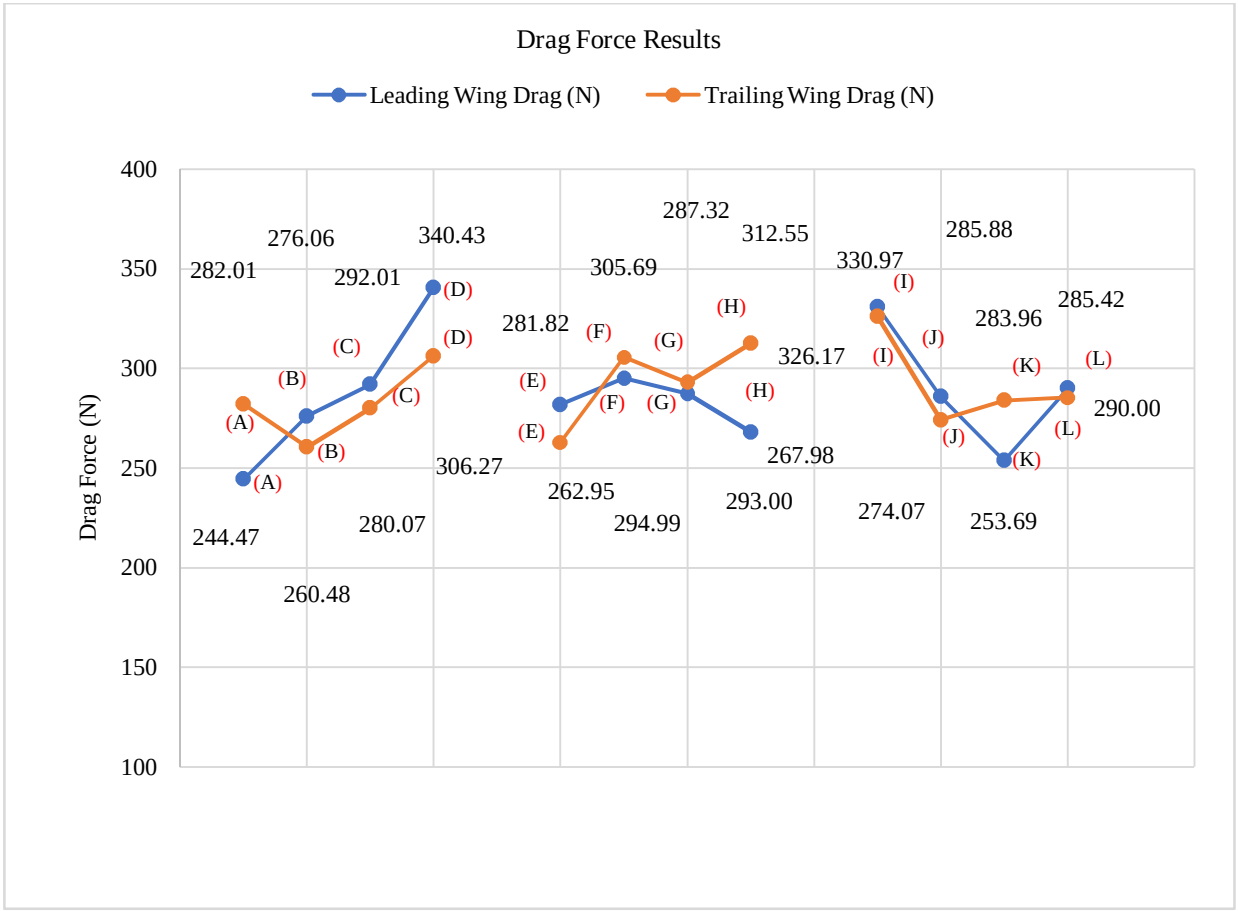

Fig.5Results of Drag Force

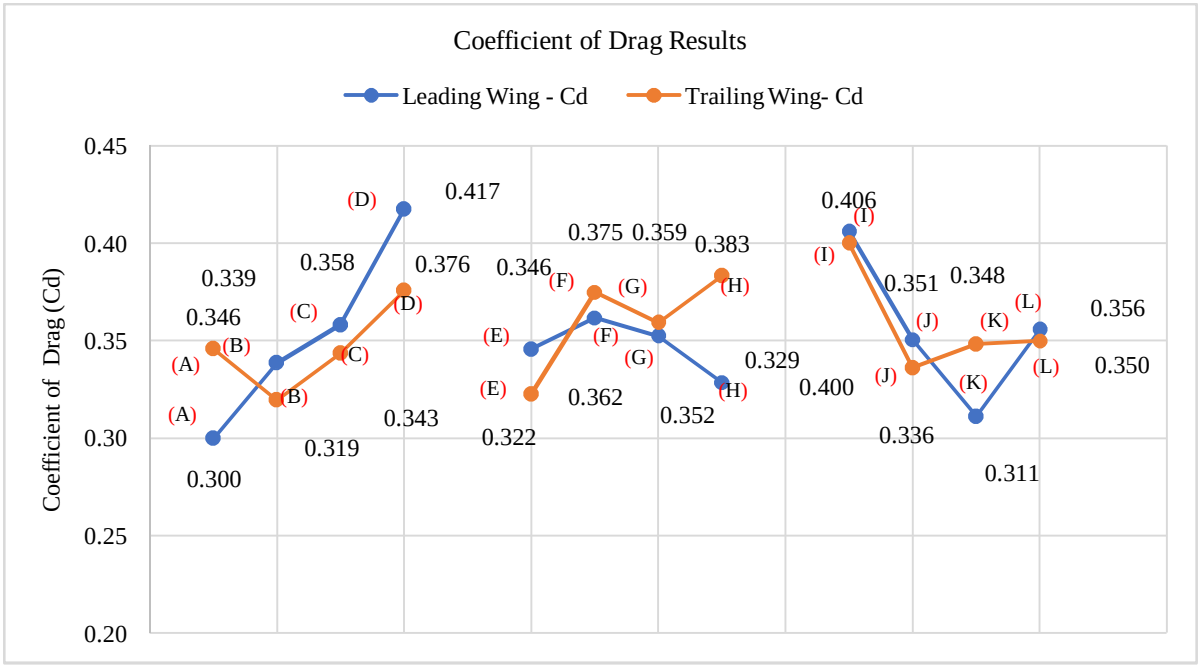

Fig.6Results of Coefficient of Drag

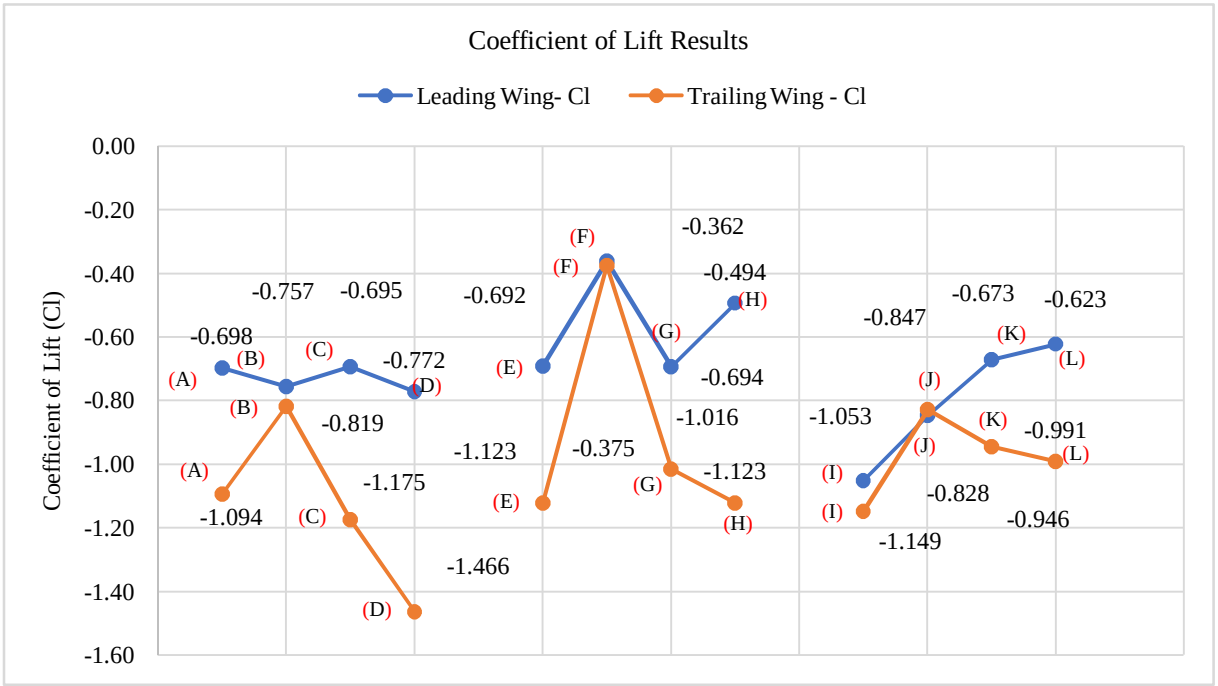

Fig.7Results of Coefficient of Lift

E. Data Judgment with Ranking Method

For ease of distinguishing the results from various wing topologies a simple ranking system was incorporated for this study. As, the main parameters that affect dirty air are downforce (N) and drag force (N), hence improvements in these parameters from the reference values were identified and ranked. In the ranking method hierarchy critical elements of investigation are both trailing and leading wings, followed by just the trailing wing and then finally just the leading wing. Table (V) has 2 columns for captured downforce and drag force values. The grey colour highlight indicates that those values are reference, green indicates improvement in the parameter and orange indicates degradation in parameter.

A specific rank point was assigned by calculating the Normalized Efficiency (E_{norm}) using the respective downforce and drag force values in all the various wing topologies. Normalization of the data was done using the range of the forces captured, as shown in equation (1.6).

$$E_{norm} = \frac{D_{norm(Downforce)}}{D_{norm(Drag\ Force)}} \qquad \text{Eq. (1.6)}$$

Using equation (1.7) the Aerodynamic Efficiency was calculated, then using equation (1.8) the normalization values (D_{norm}) for downforce and drag force were calculated. Thereafter, Normalized Wing Efficiency was calculated using the equation (1.9), mentioned below.

$$Aerodynamic\ Efficiency = \frac{Downforce}{Drag\ Force} \qquad \text{Eq. (1.7)}$$

$$D_{norm} = \frac{D - D_{min}}{D_{max} - D_{min}} \qquad \text{Eq. (1.8)}$$

Post calculating the Normalized Efficiency (E_{norm}), the data was ranked on the overall performance, as shown in the Table (X).

TABLE V
Downforce Ranking for Various Wing Topologies

Topology Name	Leading Wing Downforce (N)	Trailing Wing Downforce (N)
RW_ 3 mm_100p_0d	-569.423	-892.202
RW_ 3 mm_100p_8d	-668.044	-617.577
RW_ 3 mm_100p_16d	-566.379	-958.043
RW_ 3 mm_100p_24d	-629.722	-1195.041
RW_ 3 mm_90p_0d	-563.995	-915.632
RW_ 3 mm_90p_8d	-684.907	-989.480
RW_ 3 mm_90p_16d	-565.945	-828.442
RW_ 3 mm_90p_24d	-402.851	-915.746
RW_ 3 mm_80p_0d	-858.637	-937.051
RW_ 3 mm_80p_8d	-690.927	-675.539
RW_ 3 mm_80p_16d	-548.429	-771.014
RW_ 3 mm_80p_24d	-508.081	-808.386

TABLE VI
Drag Force Ranking for Various Wing Topologies

Topology Name	Leading Wing Drag (N)	Trailing Wing Drag (N)
RW_ 3 mm_100p_0d	244.469	282.011
RW_ 3 mm_100p_8d	276.057	260.483
RW_ 3 mm_100p_16d	292.014	280.072
RW_ 3 mm_100p_24d	340.426	306.270
RW_ 3 mm_90p_0d	281.821	262.946
RW_ 3 mm_90p_8d	294.993	305.693
RW_ 3 mm_90p_16d	287.320	292.998
RW_ 3 mm_90p_24d	267.980	312.546
RW_ 3 mm_80p_0d	330.971	326.166
RW_ 3 mm_80p_8d	285.882	274.072
RW_ 3 mm_80p_16d	253.690	283.956
RW_ 3 mm_80p_24d	289.995	285.423

TABLE VII
Calculate D_{norm}, η, E_{norm} for Leading wings

Topology	Downforce(D)	D_{norm} (Downforce)	Drag	D_{norm} (Drag)	η = D / F	E_{norm}
A	-569.423	0.3657	244.469	0.000	2.329	Undefined
B	-668.044	0.5809	276.057	0.3291	2.420	1.765
C	-566.379	0.3594	292.014	0.4961	1.940	0.724
D	-629.722	0.5074	340.426	1.0000	1.849	0.507
E	-563.995	0.3548	281.821	0.3934	2.002	0.902
F	-684.907	0.6150	294.993	0.5241	2.332	1.173
G	-565.945	0.3583	287.320	0.4469	1.970	0.801
H	-402.851	0..000	267.980	0.2447	1.504	0.000
I	-858.637	1.000	330.971	0.8991	2.595	1.112
J	-690.927	0.6266	285.882	0.4347	2.416	1.441
K	-548.429	0.3251	253.690	0.0971	2.162	3.347
L	-508.081	0.2327	289.995	0.5192	1.752	0.448

TABLE VIII
Final Ranked Table for Leading Wings (Post Calculation)

Rank	Topology	D_{norm} (Downforce)	η	E_{norm}
1	K(RW_80p_16d)	0.3251	2.162	3.347
2	B(RW_100p_8d)	0.5809	2.420	1.765
3	J(RW_80p_8d)	0.6266	2.416	1.441
4	F(RW_90p_8d)	0.6150	2.322	1.173
5	I(RW_80p_0d)	1.0000	2.595	1.112
6	E(RW_90p_0d)	0.3548	2.002	0.902
7	G(RW_90p_16d)	0.3583	1.970	0.801
8	C(RW_100p_16d)	0.3594	1.940	0.724
9	D(RW_100p_24d)	0.5074	1.849	0.507
10	L(RW_80p_24d)	0.2327	1.752	0.448
11	H(RW_90p_24d)	0.0000	1.504	0.000
N/A	A(RW_100p_0d)	0.3657	2.329	undefined

TABLE IX
Calculate D_{norm}, η, E_{norm} for Trailing wings

Topology	Downforce(D)	D_{norm} (Downforce)	Drag	D_{norm} (Drag)	η = D / F	E_{norm}
A	-892.202	0.475	282.011	0.475	3.163	1.450
B	-617.577	0.000	260.483	0.000	2.370	Undefined
C	-958.043	0.589	280.072	0.589	3.420	1.976
D	-1195.041	1.000	306.270	1.000	3.902	1.434
E	-915.632	0.516	262.946	0.516	3.483	13.764
F	-989.480	0.644	305.693	0.644	3.236	0.935
G	-828.442	0.365	292.998	0.365	2.827	0.737
H	-915.746	0.516	312.546	0.516	2.930	0.651
I	-937.051	0.553	326.166	0.553	2.872	0.553
J	-675.539	0.100	274.072	0.100	2.464	0.485

K	-771.014	0.265	283.956	0.265	2.715	0.743
L	-808.386	0.330	285.423	0.330	2.831	0.870

TABLE X
Final Ranked Table for Trailing Wings (Post Calculation)

Rank	Topology	D_{norm}	η	E_{norm}
1	C (RW_100p_16d)	0.5239	3.420	1.976
2	D(RW_100p_24d)	1.0000	3.902	1.434
3	A(RW_100p_0d)	0.4090	3.163	1.451
4	F (RW_90p_8d)	0.5724	3.236	0.935
5	L(RW_80p_24d)	0.2940	2.831	0.870
6	K(RW_80p_16d)	0.2370	2.715	0.743
7	G(RW_90p_16d)	0.3380	2.827	0.737
8	J(RW_80p_8d)	0.0975	2.464	0.485
9	H(RW_90p_24d)	0.4527	2.930	0.651
10	I(RW_80p_0d)	0.4860	2.872	0.553
N/A	E(RW_90p_0d)	0.4525	3.483	13.764
N/A	B(RW_100p_8d)	0.0000	2.370	undefined

IV. RESULTS AND DISCUSSION

A. *Leading Wing Results*

The comparative analysis between the Topology B and Topology J leading wings demonstrates clear aerodynamic improvements over the baseline Topology A configuration. Both modified designs achieved significant gains in downforce generation, increasing by 17.31% and 21.33%, respectively. The pressure contour plots and velocity magnitude distributions (see Fig. 8(A) and Fig. 8(B)) illustrate the formation of distinct low-pressure regions along the suction surfaces, indicating enhanced flow acceleration and stronger pressure differentials relative to the baseline.

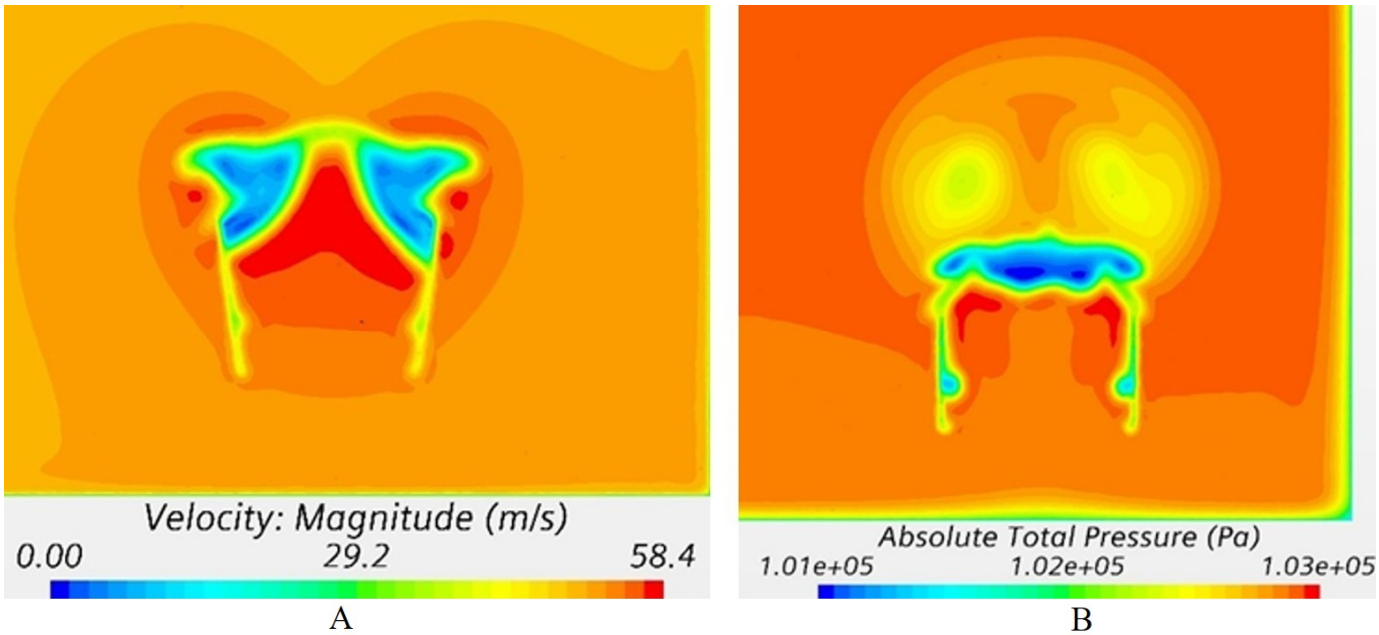

Fig. 8 Velocity magnitude (A) and absolute total pressure (B) contours for Topology B.

In Topology B, the suction region is more concentrated near the mid-span, creating localised pressure intensity that enhances downforce but introduces slight asymmetry in the pressure field.

Conversely, Topology J exhibits a broader and smoother low-pressure distribution across the chord, reflecting improved flow attachment and reduced boundary-layer separation. The velocity magnitude contours (see Fig. 10(A)) confirm these observations, showing higher airflow velocities beneath both wing surfaces, with Topology J demonstrating a more continuous and stable acceleration region. As a result, both configurations achieved an aerodynamic-efficiency improvement of 3.76–3.79%, reflecting an improved lift-to-drag balance resulting from refined geometry.

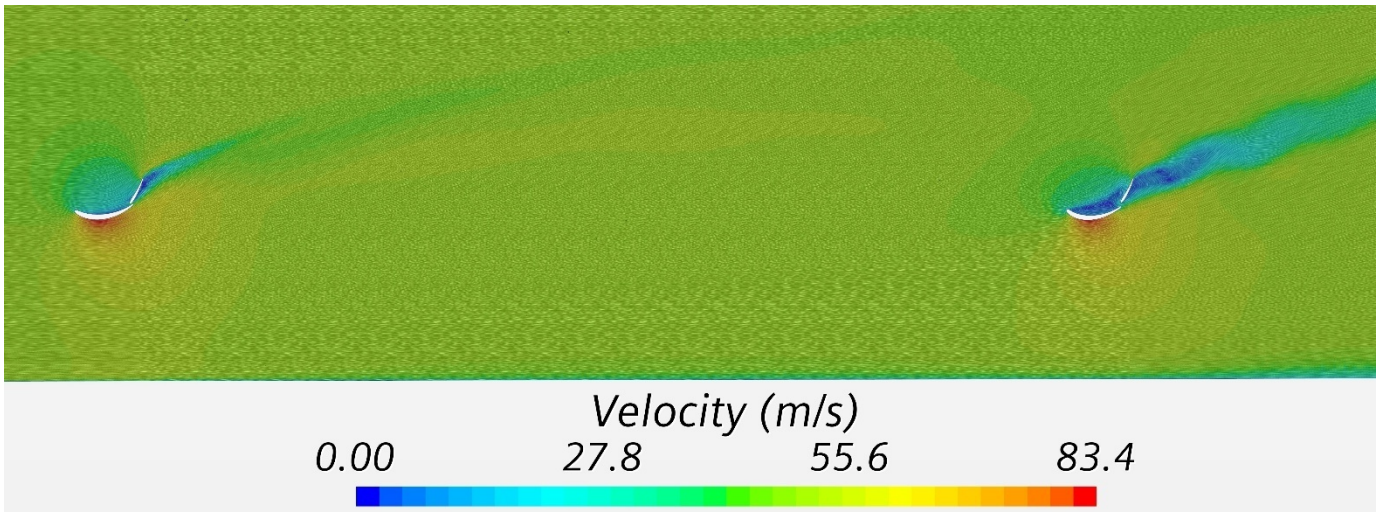

Fig.9 Velocity vector-field visualizationfor Topology B

The combined velocity and vector-field visualisation (see Fig. 9 and Fig. 11) further differentiate the aerodynamic wake characteristics of the two leading-wing configurations. Topology B produces moderate vortex formation and a slightly diffused wake pattern behind the trailing edge, indicating minor flow instability and partial separation. In contrast, Topology J presents a more coherent and streamlined wake, characterised by reduced turbulence intensity and smoother streamwise velocity transitions. This improved wake discipline enhances aerodynamic stability but incurs a drag penalty, increasing by 12.92% for Topology B and 16.93% for Topology J—consistent with the stronger induced effects generated by higher suction levels.

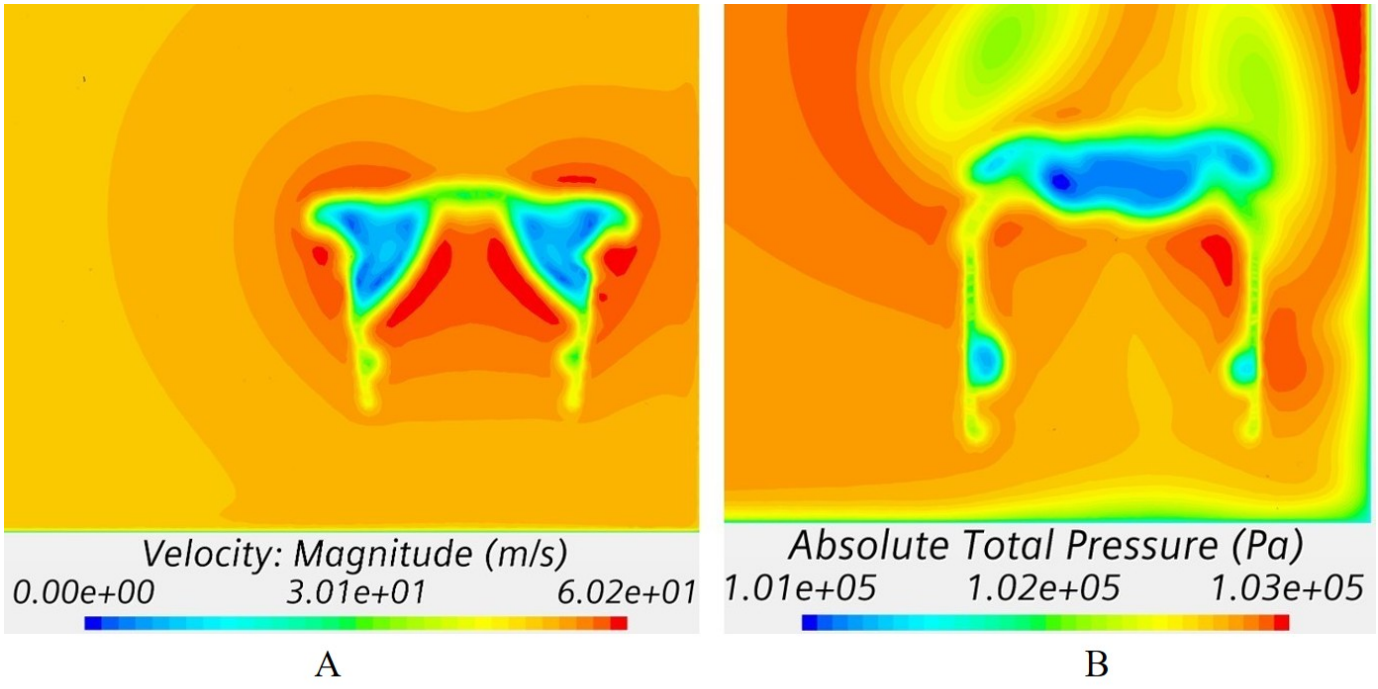

Fig. 10Velocity magnitude (A) and absolute total pressure (B) contours for Topology J

These results emphasise a fundamental aerodynamic trade-off: while Topology J achieves the highest downforce and superior wake coherence, it does so at the expense of increased induced drag. Topology B, on the other hand, maintains a more balanced aerodynamic profile, producing slightly lower downforce but with improved stability and energy efficiency. The stronger suction field generated by Topology J also results in a denser wake region (see Fig. 10(B)), which may adversely influence downstream airflow to the trailing wing, whereas the less intense wake of Topology B supports smoother flow compatibility across the multi-element assembly.

Dirty-air impact, the same suction gains that help the leader also deepen the absolute total-pressure deficit in its wake. Both B and J thicken and energise the inter-element wake delivered to the follower (see Fig. 10(B)), degrading the trailing wing's inlet quality. Quantitatively, when these wakes convict onto the trailing wing, downforce drops versus baseline A by 30.8% for B and 24.3% for J. In other words, B and J maximise the leader's load but intensify dirty air for the follower; J does so slightly more than B because its broader suction footprint produces a denser, more persistent p_o-deficit field.

These results emphasise a fundamental aerodynamic trade-off: while Topology J achieves the highest downforce and superior wake coherence on the leader, it does so at the expense of increased induced drag and harsher inflow for the follower. Topology B is marginally more balanced at the leader but still strengthens the wake relative to A. Practically, both B and J are favourable if the objective is to maximise the leading wing's load; they are unfavourable if the objective is to enable closer following, where reduced dirty-air severity at the trailing element is critical.

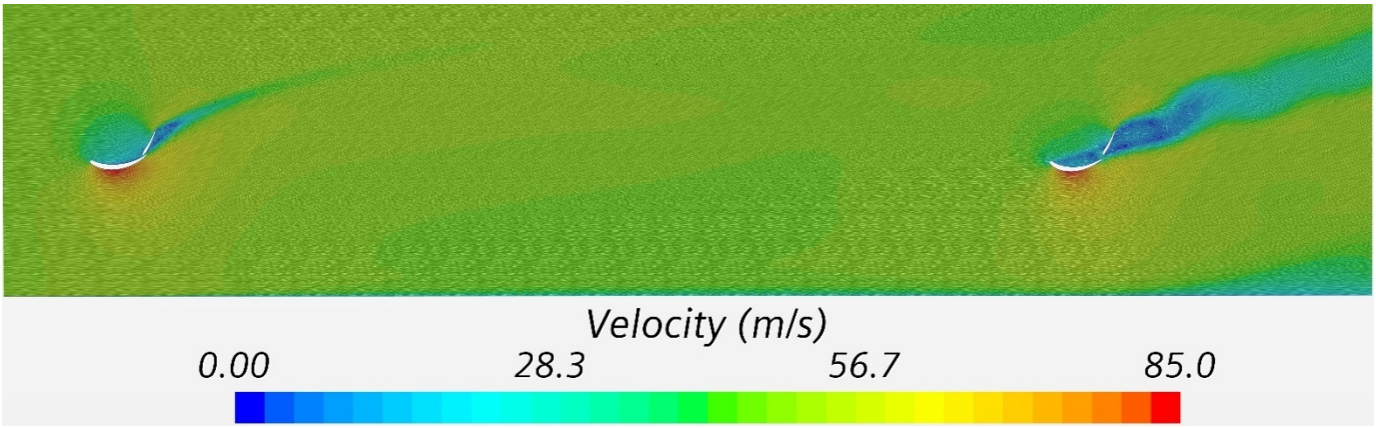

Fig.11 Velocity vector-field visualizationfor Topology J

Bigger suction on the leader strengthens circulation and downwash, deepening the absolute total-pressure (p_o) deficit and thickening the shear layer it sheds. That low-p_o, high-shear wake hits the inter-element plane with less recoverable energy and a more negative induced angle, so the follower's suction peak weakens, and pressure recovery degrades. Both B and J do this, but in slightly diverse ways. B (100%, 8°) concentrates suction near mid-span, creating a narrower wake core with a deep p_o hole and moderate vortex meandering; the trailing wing then ingests a vertically thick deficit band that clips its suction plateau. J (80%, 8°) spreads suction more evenly, so the wake is tidier but denser and wider—the p_o deficit persists farther downstream and stays aligned with the follower's span. The numbers tell the story: while the leader gains +17.31% (B) and +21.33% (J) downforce, with induced-drag penalties of +12.92% and +16.93%, the trailing-wing downforce drops vs A by 30.8% with B (−617.6 N vs −892.2 N) and 24.3% with J (−675.5 N vs −892.2 N). So, B and J are excellent if the goal is to maximise the leader's load, but they intensify dirty air for the follower—J often feeling worse across more of the span because its broader, more persistent p_o deficit leaves the follower with lower inlet energy even if the wake looks more "coherent."

B. Trailing Wing Results

The aerodynamic comparison between Topologies A, C, and E reveals distinct variations in downforce and drag performance, primarily driven by geometric downsizing and endplate optimization. The baseline configuration (Topology A) establishes the reference aerodynamic behaviour, exhibiting moderate suction intensity along the leading wing and a coherent yet diffused wake field, providing a stable inflow for the trailing element. Transitioning to Topology C results in a slight reduction in drag force by 1.939 N, accompanied by a significant 7.38% increase in downforce, indicating improved aerodynamic loading efficiency.

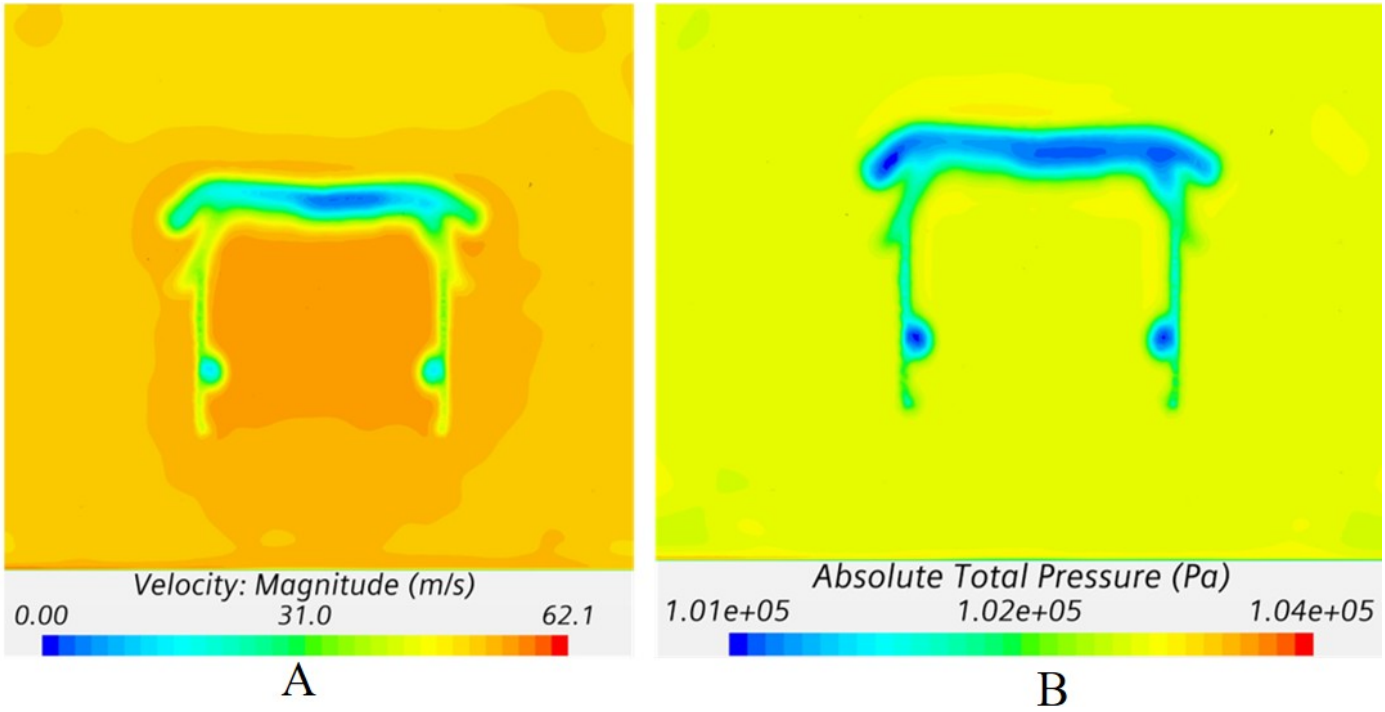

Fig. 12Velocity magnitude (A) and absolute total pressure (B) contours for Topology E

As shown in Fig. 12(A) and Fig. 12(B), the velocity magnitude and total pressure contours for Topology E highlight a broad low-pressure region across the suction surface, signifying enhanced flow acceleration and smoother reattachment. This improvement in flow stability minimizes tip-vortex strength and promotes better wake discipline, yielding more uniform pressure recovery and reduced flow separation behind the trailing edge. Consequently, the wake becomes narrower and better organized, improving downstream flow quality and contributing to a stronger lift-to-drag balance within the two-element wing system.

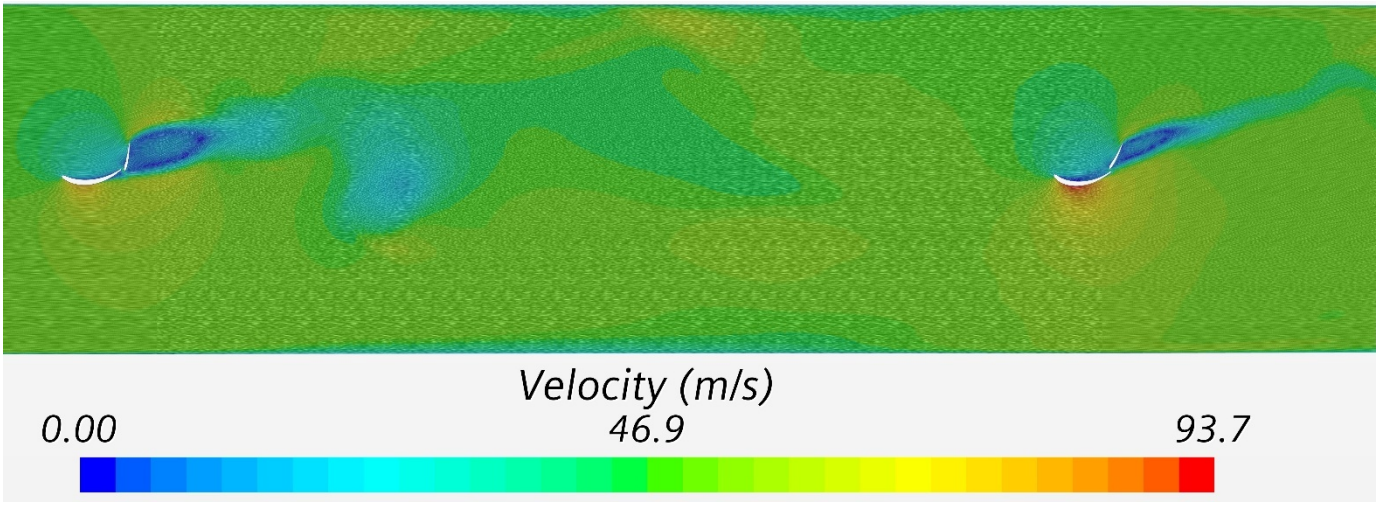

Fig 13. Velocity vector-field visualizationfor Topology E

Topology E, as visualized in Fig. 13, demonstrates the most pronounced drag reduction—19.065 N lower than Topology A—while maintaining a 2.62% increase in downforce. The streamline field in Fig. 13 depicts refined, well-structured wake formations with minimal turbulence, confirming E's superior aerodynamic discipline and pressure recovery. Correspondingly, Fig. 16(A) and Fig. 16(B) verify a smoother, continuous low-pressure region beneath the suction surface, reinforcing the configuration's ability to maintain high aerodynamic stability. Overall, E emerges as the most efficient topology among the trailing-wing cases, combining low drag with sustained downforce through optimized geometry and balanced wake control.

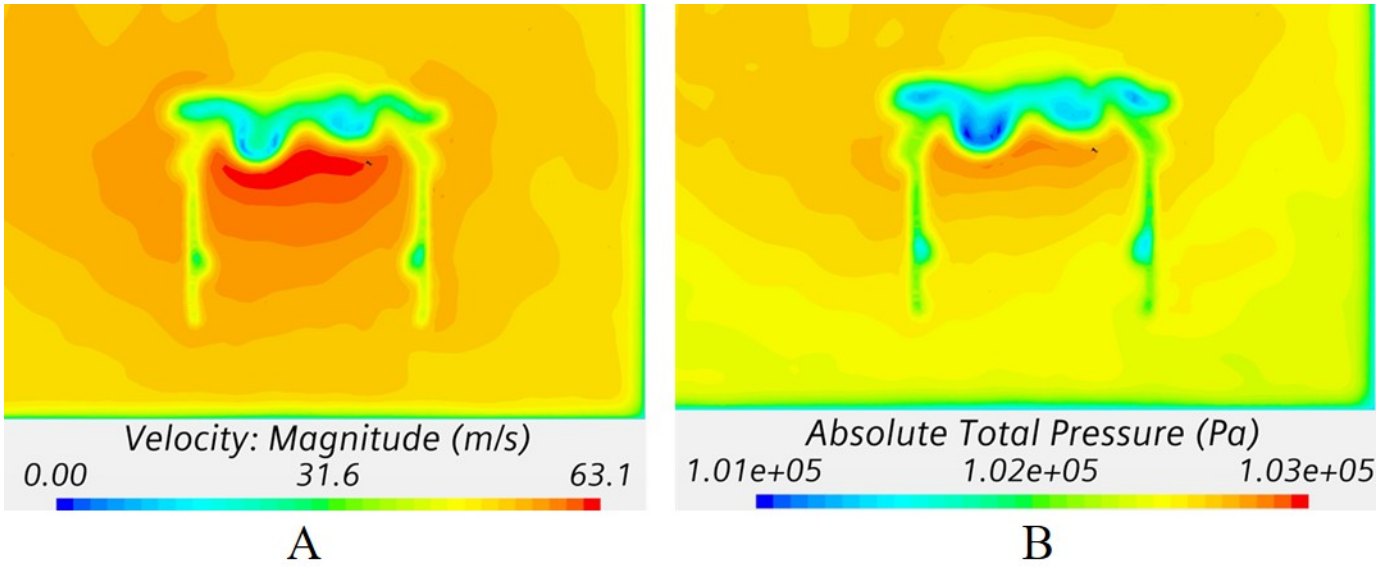

Fig. 14Velocity magnitude (A) and absolute total pressure (B) contours for Topology A

When compared with Topologies B and J, which exhibit stronger suction peaks and higher leading-wing lift coefficients, C and E achieve a more favourable aerodynamic trade-off. As evident in Fig. 14(A–B) and Fig. 15, B and J produce energetic, yet diffused wake regions characterized by elevated vortex activity and broader flow dispersion. This aggressive suction mechanism enhances local lift generation but deteriorates downstream wake uniformity, thereby degrading the aerodynamic efficiency of the trailing wing.

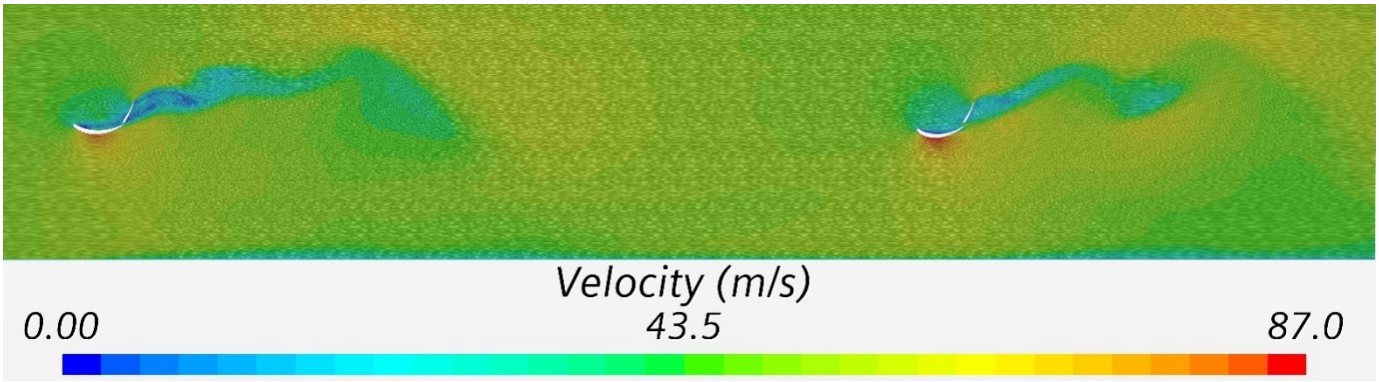

Fig 15.Velocity vector-field visualizationfor Topology A

Conversely, C and E sustain moderate suction while preserving superior wake coherence and reduced lateral flow dispersion. These characteristics foster smoother inflow to the trailing wing and greater overall system stability. The velocity field visualizations (Fig. 15–17) support this observation: B and J generate intense induced circulation with wide wake spread, whereas C and E maintain compact, well-aligned wake cores. Thus, while B and J maximize individual downforce, they compromise system-level aerodynamic harmony, whereas C and E deliver balanced performance, optimizing both downforce and wake uniformity across the entire multi-element assembly.

As demonstrated in Fig. 21–Fig. 23, variations in the leading-wing geometry directly influence the aerodynamic environment experienced by the trailing element. Moderate downsizing and controlled endplate angling (as in Topologies C and E) narrow the wake corridor and maintain higher total pressure within the inter-element flow region, allowing the trailing wing to operate under more stable and energetic inflow conditions. This leads to improved trailing-wing efficiency and reduced induced drag, enhancing downstream aerodynamic stability.

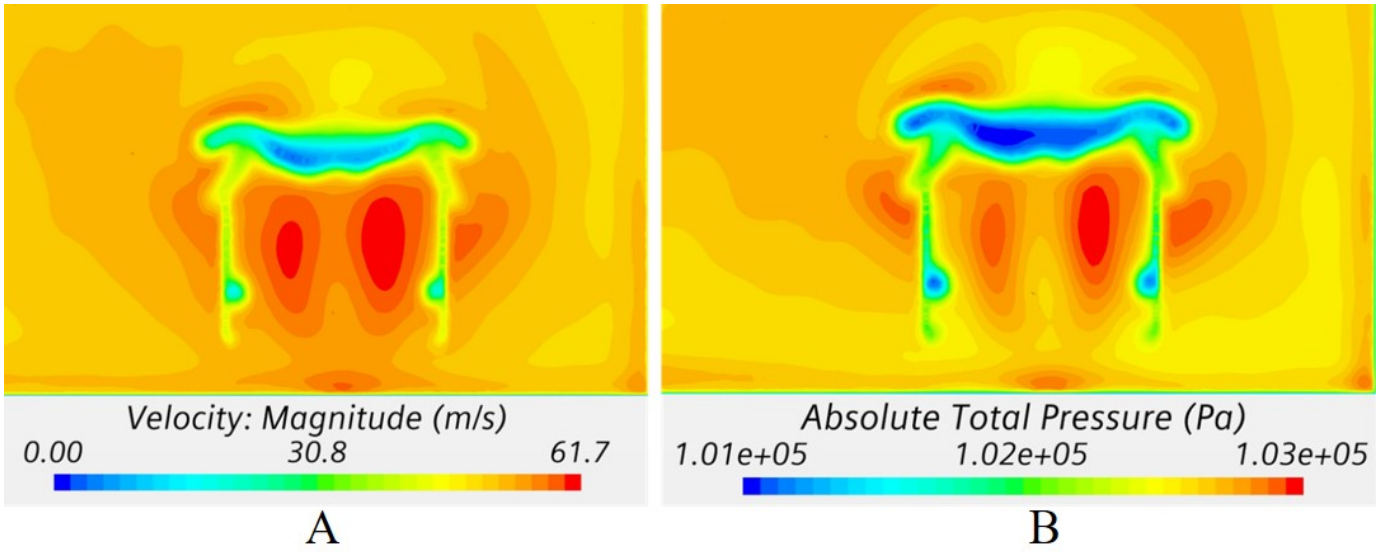

Fig. 16Velocity magnitude (A) and absolute total pressure (B) contours for Topology C

In contrast, configurations with more aggressive suction gradients (such as Topologies B and J) amplify vortex interactions, reducing pressure recovery and increasing turbulence downstream. This nonlinear aerodynamic coupling explains why certain geometric refinements (C and E) simultaneously improve drag and downforce, whereas others (B and J) achieve higher individual lift at the cost of wake quality.

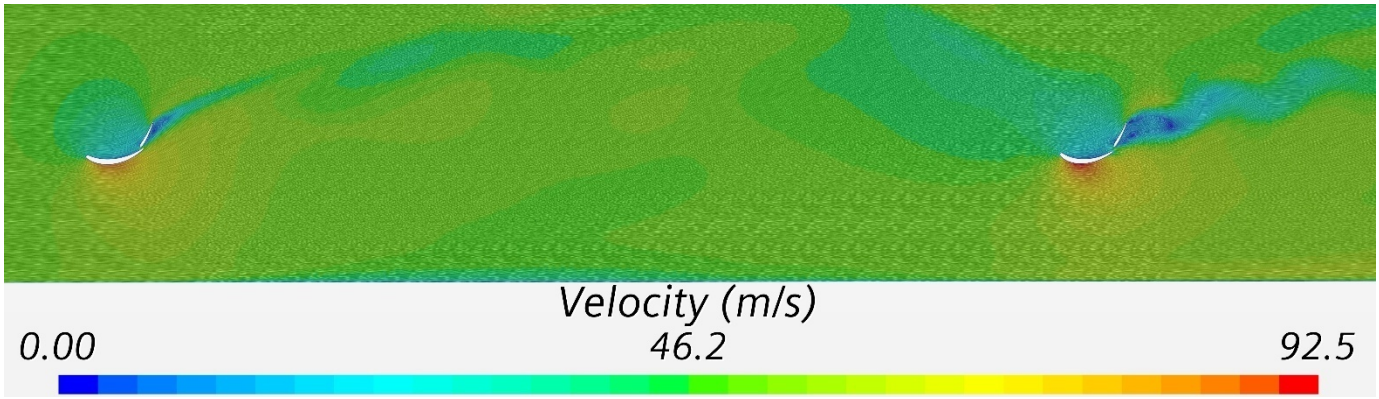

Fig 17.Velocity vector-field visualizationfor Topology C

The comparative results summarised in Table IX and Table X highlight the aerodynamic interaction trends between the leading and trailing wings. In the leading-wing rankings (Table IX), Topologies B and J rank among the top performers for normalised downforce and efficiency, while C and E occupy lower positions. However, this trend reverses in the trailing-wing rankings (Table X)—Topology C achieves Rank 1, and Topology E exhibits exceptionally high normalized efficiency, whereas B and J drop significantly in rank.

Trailing Wing Results - dirty-air focus (A, C, E vs B, J). Baseline A sets the reference: moderate leader suction produces a coherent, partly diffused wake, so the follower sees a stable, mid-energy inflow and delivers consistent load (Fig. 14(A–B), Fig. 15). C (100%, 16°) reduces dirty-air severity relative to A by tightening the wake corridor and lifting the deepest p_0 deficit away from the follower's high-leverage suction zones. The trailing wing ingests higher-energy inflow, attachment stabilises, and pressure recovery strengthens; trailing-wing downforce rises 7.38% with a small drag decrease of 1.939 N (~0.69%) (Fig. 16(A–B), Fig. 17). E (90%, 0°) also cleans the inflow, mainly via downsizing that weakens tip-vortex strength and induced downwash. The inter-element wake becomes compact and well organised (Fig. 12(A–B), Fig. 13), yielding a 19.065 N drag reduction (~6.76%) while still increasing downforce by 2.62%.

In contrast, the leader-optimised B (100%, 8°) and J (80%, 8°) deepen and widen the absolute total-pressure hole, leaving the follower with harsher inflow: trailing-wing downforce drops 30.8% with B (−617.6 N vs −892.2 N for A) and 24.3% with J (−675.5 N vs −892.2 N). Practically, replacing the B/J wake environment with C/E recovers ~36–55% of follower load at the same spacing — C vs B: +55.1% (617.6→958.0 N), C vs J: +41.8% (675.5→958.0 N); E vs B: +48.2% (617.6→915.6 N), E vs J: +35.5% (675.5→915.6 N) — while also cutting follower drag (≈0.69% for C, 6.76% for E). Against the leader-first designs B and J, C/E deliver a narrower, higher-p_0 wake to the trailing wing, which is why follower performance improves at unchanged spacing.

Topology B falls from Rank 2 in leading-wing efficiency to near the lowest tier in trailing-wing performance, while C rises from Rank 8 to Rank 1. This clear inversion highlights the aerodynamic interplay between the two wings: designs that maximize suction on the leading element (B, J) generate strong but unstable wakes that diminish trailing-wing efficiency, whereas refined configurations (C, E) promote stable flow transitions and superior overall system efficiency.

These results also confirm that no linear correlation exists between geometric parameters and aerodynamic forces. Instead, trailing-wing performance depends primarily on wake coherence, pressure-recovery strength, and induced-drag control—factors optimised when wing-size reduction and endplate angling are carefully balanced. The baseline Topology A remains aerodynamically neutral, offering moderate downforce and consistent wake formation, making it a stable benchmark. Overall, C and E achieve optimal system-level performance by prioritising flow harmony over suction magnitude, proving that aerodynamic efficiency in multi-element systems depends on balanced geometry rather than maximising the lift of individual components.

V. CONCLUSION

The findings aimed to investigate the aerodynamic performances of various topologies focusing on identifying and highlighting the reduction of dirty air for the best use cases. It also investigated how rear-wing topology influences wake quality and dirty-air effects in a tandem-wing configuration. The analysis quantified dirty air using the follower's load change relative to the baseline topology (A), supported by total-pressure and velocity-field diagnostics. The results demonstrate that no single configuration simultaneously optimises aerodynamic performance for both the leading and trailing wings.

For the leading wing, the 8° endplate geometries—Topology B (100%, 8°) and Topology J (80%, 8°)—produced the highest downforce increases of 17.31% and 21.33%, accompanied by induced-drag penalties of 12.92% and 16.93%, respectively. These strong suction fields intensified the wake's total-pressure deficit and downwash, resulting in increased dirty air for a following element. Correspondingly, the trailing wing experienced downforce losses of 30.8% (B) and 24.3% (J) relative to the baseline, confirming the detrimental wake impact of these leader-optimised designs.

In contrast, Topology C (100%, 16°) and Topology E (90%, 0°) demonstrated measurable dirty-air reduction. C narrowed the wake corridor and lifted the lowest-pressure deficit, enabling the follower to recover 7.38% additional downforce with a minor drag reduction of 1.939 N (~0.69%). E, through geometric downsizing, weakened tip-vortex intensity and induced downwash, achieving a drag reduction of 19.065 N (~6.76%) with a 2.62% downforce increase. Relative to A, these represent −7.38% and −2.62% dirty-air changes, translating to 36–55% recovery of the follower's lost load compared with B/J. From the results it was clear that there was no linear relationship between decreasing the overall size and increasing the endplate angle simultaneously, with aerodynamic improvements. However, it can be concluded that endplate angle of 8 degrees for leading wing topology was found to be the best performing among all the use cases. Similarly, for the trailing wing topologies, Topology E was the best performing of all. From the data investigated it was also concludedthat Topology E will perform betterwhen it retains full reference size or as close to that size as possible. Overall, B and J maximise leading-wing performance but intensify dirty air, whereas C and E yield cleaner wakes and greater system-level efficiency. The baseline A remains aerodynamically neutral and stable. These findings meet the study objective of identifying geometries that mitigate dirty-air effects while preserving aerodynamic balance across both elements.

There was no rear wing topology which enhanced the aerodynamic performance of both leading and trailing wings at a similar level. This indicates that one can only improve the performance of leading wing easily, whereas trailing wing optimization needs more elements to support and enhance its performance. Dirty air reduction was observed with B and J leading wing topologies, but it did not show improvement on trailing wings mainly due to it retaining the same reference wing topology.

It is clear from the data obtained that reducing size and increasing end plate angles help in improving performance. The challenging part is to find which combination works for both wings.Future work should focus on (i) mapping total-pressure deficit and turbulence-kinetic-energy decay across the inter-element region, (ii) co-optimising leading and trailing geometries with dirty-air reduction as a design objective, and (iii) exploring the 8–16° endplate-angle range at 90–100% scale to locate an equilibrium configuration capable of enhancing both leader and follower performance.

REFERENCES

[1] J. Katz, "Aerodynamics of Race Cars," *Annu. Rev. Fluid Mech.*, 2006. doi: 10.1146/annurev.fluid. (Use this as the core race-car aero text for forces, RANS/Boussinesq notes. If your copy is the 2005 preprint, keep year as in your record.)
[2] A. Buljac, H. Kozmar, and I. Džijan, "Aerodynamic performance of the underbody and wings of an open-wheel race car," *Transactions of Famena*, vol. 40, no. 2, pp. 19–34, 2016. doi: 10.21278/TOF.40202.
[3] M. D. Soso and P. A. Wilson, "Aerodynamics of a wing in ground effect in generic racing car wake flows," *Proc. IMechE Part D: J. Automobile Engineering*, vol. 220, no. 1, pp. 1–13, 2006. doi: 10.1243/095440705X69632.
[4] J. Newbon and D. Sims-Williams, "Aerodynamic Analysis of Grand Prix Cars Operating in Wake Flows," SAE Technical Paper 2017-01-1546, 2017. doi: 10.4271/2017-01-1546.
[5] M. Wilson, R. Dominy, and A. Straker, "The Aerodynamic Characteristics of a Race Car Wing Operating in a Wake," SAE, vol. 1, no. 1, 2008.
[6] J. P. Holman and J. Lloyd, *McGraw-Hill Series in Mechanical Engineering* (fundamentals used for CFD pipeline and N–S statements).
[7] M. A. R. V. Rayen, "Numerical Evaluation of Underbody Aerodynamics in F1 2022 Car," ResearchGate, 2019.
[8] T. Hughes, "CFD Study of Flow over a Simplified Car (Ahmed Body) Using Different Turbulence Models," ResearchGate, 2018.
[9] D. G. Karkoulias, E. D. Tzoganis, A. G. Panagiotopoulos, S. G. D. Acheimastos, and D. P. Margaris, "Computational Fluid Dynamics Study of Wing in Air Flow and Air–Solid Flow Using Three Different Meshing Techniques…," *Computation*, vol. 10, no. 3, 2022. doi: 10.3390/computation10030034.
[10] G. M. Le Good, J. P. Howell, M. A. Passmore, and A. Cogotti, "A comparison of on-road aerodynamic drag measurements with wind tunnel data from Pininfarina and MIRA," SAE Technical Paper 980394, 1998. doi: 10.4271/980394.
[11] Z. Wang, X. Hu, Z. Hui, G. Yu, W. Lan, and F. Liu, "Aerodynamic characteristics of MIRA automobile model based on fluid-structure coupling," *AIP Advances*, vol. 12, no. 3, 2022. doi: 10.1063/5.0083618.
[12] J. Fields, "How Advancements in Aerodynamics Improves the Performance of Formula 1 Racecars," Union Digital Works, 2015.
[13] P. Pansare, S. Chawla, P. B. Pansare, E. K. Mishra, G. Brahma, and R. Kumar, "Application of Mosaic Mesh on Store Separation Modelling and its Validation with Experimental Data," ResearchGate.
[14] D. Gogel, "The Effects of End Plates on Downforce in Yaw," SAE Technical Paper 2006-01-3647, 2006.
[15] M. S. Selig, "An Angle of Attack Correction Scheme for the Design of Low Aspect Ratio Wings With Endplates," SAE Technical Paper 2002-01-3292, 2002.
[16] M. Basso, C. Cravero, and D. Marsano, "Aerodynamic effect of the gurney flap on the front wing of a F1 car…," *Energies*, vol. 14, no. 8, 2021. doi: 10.3390/en14082059.
[17] S. Jain, N. Sitaram, and S. Krishnaswamy, "Effect of Reynolds number on aerodynamics of airfoil with gurney flap," *Int. J. Rotating Machinery*, 2015. doi: 10.1155/2015/628632.

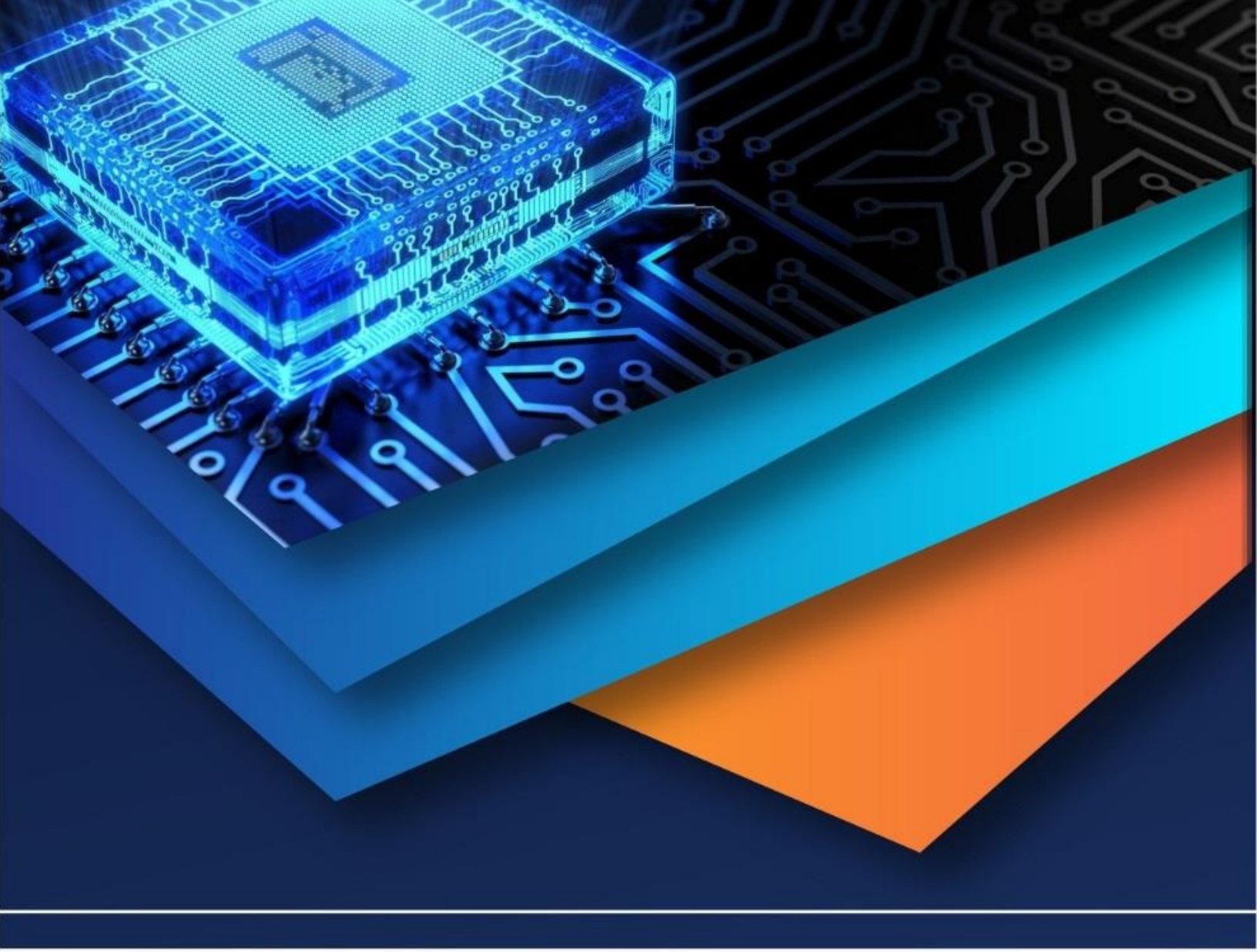

10.22214/IJRASET

45.98

IMPACT FACTOR: 7.129

IMPACT FACTOR: 7.429

INTERNATIONAL JOURNAL FOR RESEARCH

IN APPLIED SCIENCE & ENGINEERING TECHNOLOGY